

Title: Effect of hydrogen on steady-state and transient combustion instability characteristics

Authors: John Strollo, Stephen Peluso, Jacqueline O'Connor

Affiliation: Pennsylvania State University, University Park, PA, USA

ABSTRACT

This paper examines the effects of steady-state and transient hydrogen enrichment on thermoacoustic instability in a model gas turbine combustor. Combustion instability, a feedback loop between flame heat release rate oscillations and combustor acoustics, is characterized in a swirl-stabilized flame operated at a range of hydrogen-natural gas fuel blends and heat rates. Measurements of combustor chamber pressure fluctuations and CH* chemiluminescence imaging are used to characterize instability at a range of operating conditions. Steady-state tests show that both mixture heat rate and hydrogen content affect system stability. At a given heat rate, higher levels of hydrogen result in unstable combustion. As heat rate increases, instability occurs at lower concentrations of hydrogen in the fuel. Transient operation was tested in two directions – instability onset and decay – and two hydrogen-addition times – a short time of 1 millisecond and a longer time of 4 seconds. Results show that instability onset processes, through the transient addition of hydrogen, are highly repeatable regardless of the timescale of hydrogen addition. Certain instability decay processes are less repeatable, resulting in cases that do not fully transition from unstable to stable combustion despite similar changes in hydrogen fuel flow rate. Flame behavior before, during, and after the transient is characterized using high-speed CH* chemiluminescence imaging. Analysis of the high-speed images show changes in flame stabilization and dynamics during the onset and decay processes. The results of this study can have implications for systems

that experience variations in fuel composition, particularly in light of growing interest in hydrogen as a renewable fuel.

KEYWORDS

thermoacoustic instability, transient operation, hydrogen enrichment

NOMENCLATURE

A	Initial amplitude asymptote [kPa]
B	Final amplitude asymptote [kPa]
$CoHR$	Center of heat release [mm]
F	Final state
I	Initial state
IQR	Inner quartile range
N	Number of pixels
$Q1-Q4$	Quartiles 1-4
\dot{Q}	Heat rate [kW]
RMS	Root-mean-square
T_{in}	Combustor inlet temperature [C]
k	Exponential value
r	Radial coordinate [mm]
t	Time [s]
t_o	Time value of curve center [s]
x	Axial coordinate [mm]
x	Mole fraction

$\tilde{\epsilon}_i$	CH* intensity at i^{th} pixel
τ	Combustor characteristic timescale [ms]
Φ	Equivalence ratio

INTRODUCTION

In an effort to reduce pollutant and CO₂ emissions in gas turbines, hydrogen has been identified as a renewable fuel source that can be added in various quantities to existing gas turbine fuels. Hydrogen-rich fuels can offer reductions in CO and CO₂ emissions, while also offering potential increases in turbine efficiencies and outputs [1]. One of the most exploitable benefits of these blends is the high flame speed of hydrogen-rich flames [2]. These increased flame speeds have been shown to extend lean operating ranges [3,4], increase reaction zone intensity [3], and reduce CO emissions without significant changes to NO_x emissions [4]. Increased consumption speeds can also reduce the residence time needed to accommodate the flame, allowing for leaner operation [5].

Understanding the full span of chemical and physical effects of hydrogen enrichment can provide valuable information regarding the use of hydrogen in gas turbine engines. The effects are particularly important in the case of lean-burn, low-NO_x gas turbines where combustion instability may arise. Combustion instability is a potential issue that is caused by a feedback loop between combustor acoustics and heat release rate oscillations. These instabilities can cause gas turbine component damage, generate unwanted noise, and diminish emissions performance.

Previous studies have identified the mechanisms that contribute to the formation of combustion instabilities [6]. Interactions between combustor acoustics and heat release rate oscillations can be

driven by a number of coupling mechanisms, including velocity coupling [6,7] and mixture-composition coupling [6,8]. In this study, combustion instability is largely driven by velocity coupling, where acoustically-driven vortical structures cause fluctuations in flame heat release rate [7]. In order to fully quantify the benefits and drawbacks of hydrogen enrichment, the effects of hydrogen enrichment on these interaction mechanisms must be studied further.

Hydrogen enrichment has been shown to activate different instability mechanisms and alter the phase difference between heat release rate and combustor acoustics. Phase alteration can either inhibit [5,9,10] or enhance [11–13] combustion instabilities. For example, a study by Hong et al. [9] showed that hydrogen addition to a propane flame reduced the phase coupling between pressure and heat release. This study also showed that transitions to instability modes occurred at leaner equivalence ratios as more hydrogen was added. Alternatively, a study by Zhang and Ratner [13] showed that hydrogen enrichment can cause increased flame wrinkling. This increased wrinkling can result in increased flame area changes and thus enhanced combustion instabilities. These and other studies [5,9–14] show that depending on combustor characteristics, hydrogen enrichment and fuel composition can have different effects on combustion instability. In an effort to further investigate the mechanisms that cause these variable results, recent studies have observed hydrogen enrichment effects on strain, flow field, and peak heat release locations.

Recent hydrogen enrichment studies on flame response to strain have uncovered benefits to hydrogen usage, such as increased flame speed [2,15], burn rate [15,16], and extinction strain rate [15,17]. One study by Altay et al. [5] showed that increases in hydrogen content made flame consumption speed less responsive to variations in strain. This means that reaction rate and flame speed were less dependent on strain, a result also demonstrated in [18] through Lewis number reduction. Another study by Wicksall et al. [19] showed that the chemical effects of hydrogen

enrichment caused flame reaction zones to be less influenced by the flow field. These chemical effects allowed the flame to be more resistant to strain. The strain effect studies described above show that hydrogen addition can allow flames to exist in adverse, high velocity environments.

Further investigation of hydrogen enrichment effects on combustor flow fields have elevated understanding of flame-flow coupling. Work by Hong et al. [20] showed that reaction zone structure and strained consumption speed changes are important factors for determining flame stability. Specifically, fuel composition had significant impacts on reaction zone structure and eddies in the combustor flow field. Distortion of these eddies at certain equivalence ratios and hydrogen compositions led to thermoacoustic coupling. This work highlighted that velocity fields can have direct effects on flame kinetics and temperature fields. Another flow structure analysis by Wicksall et al. [21] showed that hydrogen-enriched flames had steadier heat release than pure methane flames. Changes in recirculation zone size and flame location [17] can also contribute to reaction zone structure and consumption speed as hydrogen is added to a fuel mixture. The location changes of important aspects of a flame through flame-flow interaction can have significant implications on flame stability.

Recent hydrogen enrichment studies have shown that the location of peak heat release rate can change with fuel composition and therefore affect stability transitions. Hydrogen enrichment has been shown to shift the peak heat release location further upstream in the combustor [22], which can reduce perturbation convection times [23]. Reduction of disturbance convection times can alter the phase relationship between heat release and acoustic oscillations, causing transitions to stability or instability [24].

To date, most studies of instabilities in hydrogen-enriched flames have considered the steady-state operation of the combustor. In practice, the composition of the fuel may change over time

[25]. Recent work on the transient behavior of thermoacoustically-unstable combustion systems has provided insight into the importance of transient direction and timescale. Two types of transient studies have been conducted: those that prescribe the transient operation by varying some combustor operating condition, like equivalence ratio or fuel staging [26–29], and those that operate near a stability bifurcation point and observe the natural, noise-driven transition from one operational state to the next [30,31]. The current study falls into the first category, where variations in the fuel composition are prescribed.

The final state of combustor stability after a prescribed transient has been shown to be dependent on the timescale over which the transient is executed [26–29]. Work by Bonciolini and Noiray [27] showed that different ramping times of a bifurcation parameter resulted in different combustor end states. This work used variations in air flow rates to control changes in equivalence ratio. The combustor behavior was represented as a pair of mirrored Hopf bifurcations, where an unstable state was present between two stable states as air flow rate was increased. This study highlighted the significance of transient timescales by showing that if air flow rate ramping times were quicker than characteristic growth rate times, instability avoidance was possible.

The current work follows our previous work on transient operation in both single- and multi-nozzle combustor configurations. Transient equivalence ratio variation in a single-nozzle combustor conducted by Chen et al. [32] showed the existence of a critical equivalence ratio at which stability transitions occur. Comparisons of single-nozzle and multi-nozzle transients in a natural gas combustor showed that higher amplitude decay transients yielded shorter transition timescales, while onset timescales were fairly consistent [29,33]. In the works described in this section and beyond, “decay timescales” and “onset timescales” refer to the time it takes the instability amplitude to reach $\frac{A-B}{e}$, where A is the limit-cycle instability amplitude, B is the stable

amplitude after the transient, and e is the mathematical constant. The multi-nozzle configuration was found to be more sensitive to transient direction, suggesting that flame-flame interaction plays an important role in stability transitions. Further research on the same multi-nozzle combustor by Culler et al. [33] showed that higher staging amplitudes reduced variability in oscillation amplitudes. Decay timescales were also found to be shorter than rise timescales. Staging of the center nozzle of the multi-nozzle combustor caused phase cancellation between flames, resulting in a stabilizing effect on the combustor [33,34]. Samarasinghe et al. [34] also showed that this phase cancellation is a result of phase alteration of a convective instability in the center nozzle.

The literature described above has shown that hydrogen enrichment offers a number of benefits in terms of emissions and flame characteristics. However, varying results pertaining to hydrogen enrichment effects on combustion instabilities highlight the need for continued research in this area. In addition, research on the transient effects of fuel composition variation is sparse. Most of the existing fuel staging work has been limited to either steady-state staging with syngas [14], steady-state and transient addition of hydrogen jets [35], or transient fuel staging with natural gas [26–29]. This work examines the effects of steady-state and transient hydrogen-enrichment on the thermoacoustic stability of a model gas turbine combustor. The goal of this work is to bridge the gap between prior research on transient time effects and steady-state hydrogen addition effects on combustion instability by using hydrogen as a source for fuel-composition transients.

EXPERIMENTAL OVERVIEW

Experiments are conducted in the single-nozzle configuration of a multi-nozzle combustor, described in detail by Samarasinghe et al. [36] and shown in Figure 1(a). As described by Chen et al. [29], the single-nozzle configuration uses the center nozzle of the multi-nozzle configuration. The main difference between the two configurations is the diameter of the quartz liner; for the

multi-nozzle configuration, the diameter is 26 cm and for the single-nozzle configuration, the diameter is 11 cm. The dump ratio of the single-nozzle configuration was chosen to match the effective dump ratio of the five nozzles in the multi-nozzle configuration; previous studies have shown in this experiment [37] and others [38] that flame angle similarity is important for capturing the dynamics of multi-nozzle systems in a single-nozzle combustor. The quartz combustor liner is open-ended, meaning that combustion occurs at atmospheric pressure.

The nozzle is an industrial-scale swirl nozzle with a recessed centerbody, as shown in Figure 1(b). Air is delivered by a compressor at 2068 kPa (300 PSI) and preheated by a 50 kW process air heater such that the air is delivered at 200 °C. A Sierra Instruments 780S mass flow meter is used to measure the air flow rate, and is controlled using a needle valve. Teledyne-Hastings HFM-301 and HFM-D-301 thermal mass flow meters are used to measure the natural gas and hydrogen flow rates, respectively. The natural gas flow is controlled by a needle valve. The hydrogen flow is controlled by a needle valve for steady-state testing and a solenoid valve for transient testing.

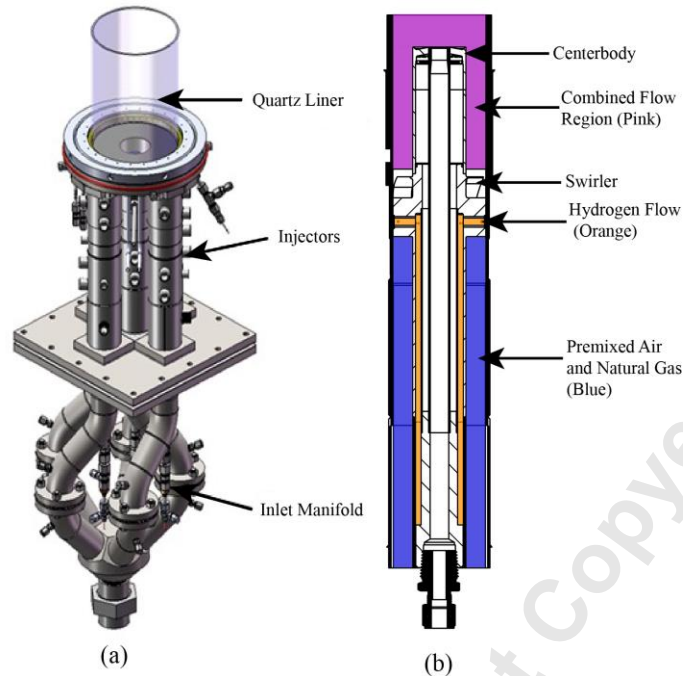


Figure 1. (a) Single nozzle combustor model and (b) detail of hydrogen injection location.

Fuel composition changes are achieved by injecting hydrogen into the partially-premixed fuel path of the nozzle. The nozzle consists of an annulus, a swirler, and a centerbody, as pictured in Figure 1(b). Natural gas and air are mixed ahead of a choke plate located far upstream of the combustor. This ensures that the natural gas and air are fully premixed. Premixed natural gas flows through the annulus of the nozzle, while hydrogen is injected just below the swirler. Hydrogen is introduced into the premixed mixture through small holes in the swirler. The hydrogen mixes with the premixed natural gas and then flows toward the flame. The hydrogen injection point is roughly 0.1 m upstream of the dump plane and is therefore considered technically premixed. While the hydrogen is technically premixed, it is well mixed with the main flow by the time it reaches the dump plane, as evidenced by acetone-PLIF measurements obtained by Orawannukul [39].

In this study, we consider both the steady-state and transient operation of this combustor. Steady-state tests are achieved by manually setting the flow rates of natural gas and hydrogen to

achieve the desired operating condition. Fuel composition transient tests are achieved by first manually setting the natural gas flow rate and then altering the hydrogen flow through a Humphrey ProControl PC3 proportional control valve. This valve is controlled using an analog constant-current supply circuit and a National Instruments data acquisition system. This configuration allows for variations in total hydrogen flow rate, transient direction (opening the valve to add hydrogen or closing the valve to subtract hydrogen), and transient time (the rate at which the valve is opened or closed).

K-type thermocouples are used to measure the centerbody temperatures at the start and end of every test. A water cooled, recess mounted, PCB dynamic pressure transducer mounted in the center nozzle is used to measure pressure fluctuations within the combustor. Dump plane pressure fluctuation amplitude data is obtained by assuming plane-wave propagation from the center nozzle transducer to the dump plane [40]. This method was validated in the multi-nozzle configuration, where a dump plane pressure transducer is available for comparison. Data is acquired at two different sampling rates, 16393 Hz and 16000 Hz. The pressure data is high-pass filtered to retain all data above 10 Hz.

A Photron SA4 high speed camera equipped with an Invisible Vision UVi 1850-10 intensifier, a Nikon AF Micro-Nikkor 60mm f/208 lens, and a 432 \pm 5 nm bandpass filter is used to obtain high speed CH* chemiluminescence images. CH* is used as an indicator of combustor heat release rate locations [41]. The images are captured at 4000 frames/second, and each combustor state is recorded for 2 seconds, yielding a frequency resolution of 0.5 Hz. The spatial resolution of the captured images is 0.33 mm/pixel.

Steady-State Data Analysis

A steady-state stability map was generated for various combustor heat rates and hydrogen percentages. Heat rates were selected to match a natural gas flame at various equivalence ratios. However, it should be noted that while heat rate can be held nominally constant, substitution of hydrogen for natural gas slightly lowers the overall equivalence ratio of the mixture. Each test consisted of 8 seconds of pressure data, yielding a frequency resolution of 0.125 Hz. The root-mean-square (RMS) of the pressure fluctuations are calculated within a range of ± 5 Hz about the peak oscillation frequency. This is done by generating the single-sided spectral density from the linear spectrum of the pressure time series, retaining ± 5 Hz about the peak oscillation frequency, then rectangularly integrating the result. Finally, the square root of the result is taken to yield the RMS value. In order to be considered sufficiently unstable, the RMS of the combustor pressure fluctuations must be at least 0.5% of the mean combustor pressure, which in this configuration is 0.483 kPa (0.07 PSI). The combustor pressure must also have a peak spectral density amplitude that is 30 times greater than the average of all other amplitudes to ensure that the instability is tonal.

Each image set consisted of 2 seconds, or 8000 frames, of CH^* data. The CH^* images are median filtered to reduce “salt and pepper” noise and smoothed using a 5 pixel by 5 pixel moving-average filter. Each image set is averaged to generate a mean flame position image. The RMS of these image sets is also obtained by calculating the RMS of the intensity at each pixel in the image. Since the images are symmetric, the mean and RMS images are Abel Inverted to account for the line-of-sight nature of the CH^* imaging technique.

Using the Abel Inverted time-averaged images, the location of the center of heat release rate was calculated. To calculate this location, the top 10% of the CH^* intensity values for each image was considered and each of these values was weighted based on radial and axial location; this

method was adapted from work by Bunce [42]. The equations for axial and radial center of heat release locations can be seen in Equations (1) and (2), where $\tilde{\epsilon}_i$ is the CH* intensity value, x is the axial coordinate, and r is the radial coordinate.

$$x_{CoHR} = \frac{\sum_{i=1}^N \tilde{\epsilon}_i x_i}{\sum_{i=1}^N \tilde{\epsilon}_i} \quad (1)$$

$$r_{CoHR} = \frac{\sum_{i=1}^N \tilde{\epsilon}_i r_i}{\sum_{i=1}^N \tilde{\epsilon}_i} \quad (2)$$

Transient Data Analysis

Once stability map results were obtained, three transition cases were selected for transient testing, based primarily on the repeatability of the transition. Transient testing was conducted in two directions: the onset direction and the decay direction. The onset transient begins with stable operation and then transitions to instability upon sufficient addition of hydrogen. The other transient direction, the decay direction, begins in unstable operation and then transitions to stable operation upon sufficient subtraction of hydrogen. Transient testing was also conducted over two control valve opening and closing times: 1 ms and 4 s. The 1 ms valve time simulates a step transient, while the 4 s valve time simulates a more gradual ramp transient. These valve times and transient directions were chosen to compare initial and final combustor states. Step transients are achieved by changing the solenoid valve position to change as fast as the hardware will allow. Step transients are commanded over a 1 millisecond window, but the hardware responds over 5 to 8 milliseconds. To maximize repeatability, care is taken to ensure that the combustor is at similar temperatures for each transient test. Centerbody temperatures vary by no more than 10 °C for the start of each transient test. Table 1 contains relevant experimental parameters for each test.

Table 1. Important experimental parameters.

Parameter	Value
Inlet Temperature	200 C
Inlet Velocity	26 m/s
Inlet Reynolds Number (Re_d)	17,000
Nozzle Swirl Number	0.7
Air Flow Rate	50.18 SCFM

The initial and final pressure fluctuation amplitudes along with the characteristic growth and decay timescales are calculated by fitting a logistic fit model to the Hilbert envelope of the pressure signal, described in detail by Culler et al. [33]. The logistic equation can be seen in Equation 3, where $P'(t)$ is the pressure oscillation amplitude (calculated from the pressure envelope), A is the initial asymptote, B is the final asymptote, k is an exponential rate, and t_0 is the curve center value. This regression method was chosen because it accurately captures the behavior of a system with two asymptotes: one at stable operation, and one at unstable operation. This method was also chosen because it is not sensitive to the start and end points of the fit [33].

$$P'(t) = \frac{A - B}{(1 + e^{k(t-t_0)})} + B \quad (3)$$

For transient testing, a total of 16 s of pressure data was recorded for each test; procedures for obtaining data are outlined in Figure 2.

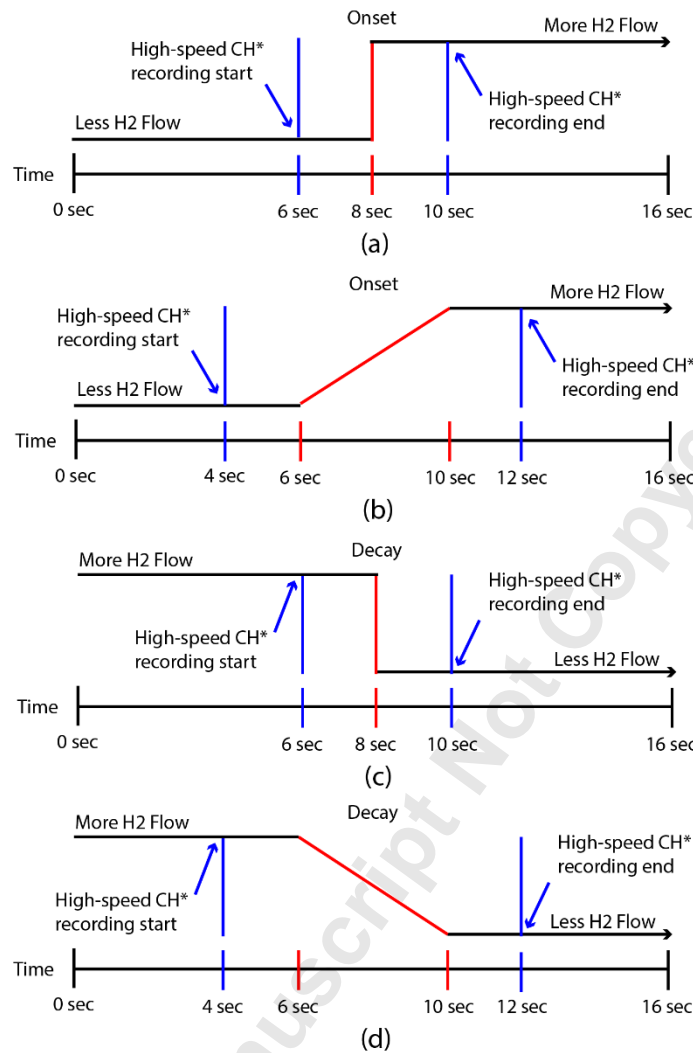


Figure 2. Transient schedules for (a) 1 ms onset, (b) 4 s onset, (c) 1 ms decay, and (d) 4 s decay cases showing hydrogen flow and CH* image capture over time.

For the 1 ms valve time, pressure data was recorded such that there was 8 s of data before the transient, and 8 s of data after the transient. When CH* images were recorded for this valve time, 4 s, or 16000 frames of CH* data were taken, centered around the valve transient. For the 4 s valve time, pressure data was recorded such that there was 6 s of data before the transient, and 6 s of data after the transient. When CH* images were recorded for this valve time, 8 s, or 32000 frames of

CH* data were taken. These image sets were also centered around the transient, such that 2 s, or 8000 frames, were recorded both before and after the transient.

RESULTS

Steady-state results

A steady-state combustor stability map was generated to determine the response of the combustor to fuel composition changes. Operating conditions were varied in terms of heat rate (41.47-62.21 kW nominal, corresponding to a natural gas flame at $\Phi=0.5-0.75$ in increments of 0.05) and hydrogen mole fraction (0-0.4 nominal, in increments of 0.1). One to three tests were run at each condition, with a focus on conditions near the stability boundary. Three tests were run for operating conditions on each side of the stability boundary at a given heat rate, termed a “stability pair,” with the exception of the natural gas-only transition from 53.92 kW to 58.06 kW. This condition was only run twice since it corresponds to an equivalence ratio transition of 0.65-0.7 and has been characterized extensively by prior work on this combustor [28,29,32–34]. Results from this parameter sweep can be seen in Table 2. The dominant frequency was calculated by determining the frequency with the maximum power spectral density. Between tests at each operating condition, the standard deviation in the pressure amplitude was 0.0600 kPa (0.0087 PSI) and in frequency was 5.05 Hz, indicating that operating conditions were repeatable across multiple test days.

Table 2. Stability map with stable (green) and unstable (red) conditions at a range of thermal powers (rows) and natural gas-hydrogen mixtures (columns). Gray boxes indicate unavailable conditions.

$T_{in}=200^{\circ}\text{C}$	xNG:xH2				
Q_{dot} (kW)	1.0:0.0	0.9:0.1	0.8:0.2	0.7:0.3	0.6:0.4
41.47		0.0039psi	0.005psi	0.0122psi	0.1620psi 460.21Hz
45.62	0.0052psi	0.0078psi	0.0501psi	0.1741psi 463.30Hz	0.1328psi 488.64Hz
49.77	0.0066psi	0.0333psi	0.1474psi 466.51Hz	0.1065psi 484.14Hz	0.1665psi 510.28Hz
53.92	0.0209psi	0.0412psi	0.2205psi 525.50Hz	0.1798psi 538.30Hz	0.0912psi 540.55Hz
58.06	0.2709psi 522.35Hz	0.2565psi 537.46Hz	0.2230psi 548.55Hz	0.1930psi 564.68Hz	0.1503psi 578.07Hz
62.21	0.2750psi 541.80Hz	0.2387psi 557.06Hz	0.2290psi 568.94Hz	0.2109psi 578.69Hz	

Table 2 shows that increases in hydrogen concentration cause transitions to instability. As heat rate increases, it takes significantly less hydrogen to cause instability. The results from the stability map also show that increases in both heat rate and hydrogen concentration result in increases in frequency of oscillation. Using ANSYS CHEMKIN [43] and GRIMech 3.0 [44], it was determined that increases in frequency were a result of increases in sound speed in the combustion products. Table 2 also shows that for all heat rates except 41.47 kW and 49.77 kW, increases in hydrogen concentration after transition to instability appear to reduce the RMS of the pressure oscillations at the dominant frequency.

In order to further investigate the mechanisms of instability at steady-state conditions, high-speed CH* images were captured for three transition pairs. The first transition pair, termed Case I for the remainder of this paper, has a nominal heat rate of 53.92 kW (natural gas flame equivalent of $\Phi=0.65$) and hydrogen mole fractions from 0.1 to 0.2. The second transition pair, termed Case II, has a nominal heat rate of 49.77 kW (natural gas flame equivalent of $\Phi=0.6$) and hydrogen mole fractions from 0.1 to 0.2. The third transition pair, termed Case III, has a nominal heat rate of 45.62 kW (natural gas flame equivalent of $\Phi=0.55$) and hydrogen mole fractions from 0.2 to 0.3. These

three cases were chosen because of their high degree of repeatability. Abel-inverted, time-averaged and RMS CH* images can be seen in Figure 3, where there are two different color scales: one that is used for all time-averaged images and one that is used for all RMS images.

The time-averaged images in Figure 3 show that flame height generally increases with reduction in heat rate. This is likely due to decreases in reactivity and flame speed associated with lower equivalence ratios. This trend is particularly notable when comparing Case I and Case II, since these cases use the same hydrogen mole fractions at different heat rates. Comparison of Case II and Case III seems to show that this trend is counteracted to some degree by the increased hydrogen mole fractions of Case III. Analysis of Case II and Case III images shows that while lower heat rates result in longer flames, increased hydrogen mole fraction tends to reduce flame height, resulting in similar flame heights between Case II and Case III.

The time-averaged images also show reduction in CH* intensity when the flame transitions to instability. This is likely a result of increased hydrogen concentration (and consequently, a reduction in natural gas composition). This change in fuel composition reduces the amount of methane available to form CH radicals and therefore reduces the intensity of CH* chemiluminescence. Regardless, the CH* technique still provides a strong representation of the heat release rate and reaction zone locations in the combustor for each condition. Reduction in CH* is also seen with reduction in heat rate at a given hydrogen concentration, as expected [41].

The RMS images in Figure 3 show that the peak fluctuation in the flame occurs in the outer recirculation zone. This is a result of vortex shedding in this region during instability as well as flame interaction with the quartz liner. These images also reveal the presence of a “nodal line” between the central recirculation zone and the outer recirculation zone at both stable and unstable conditions. This nodal line appears in the form of a minimum fluctuation intensity value between

these two zones and delineates the two primary oscillation zones in the flame. These two primary fluctuation zones appear to be due to vortex rollup in the outer recirculation zone and subsequent extinction events occurring above the vortex impingement location along the wall. The nodal line becomes more pronounced at higher heat rates and during unstable conditions, indicating that the neighboring wall-impingement and recirculation regions of the flames oscillate intensely.

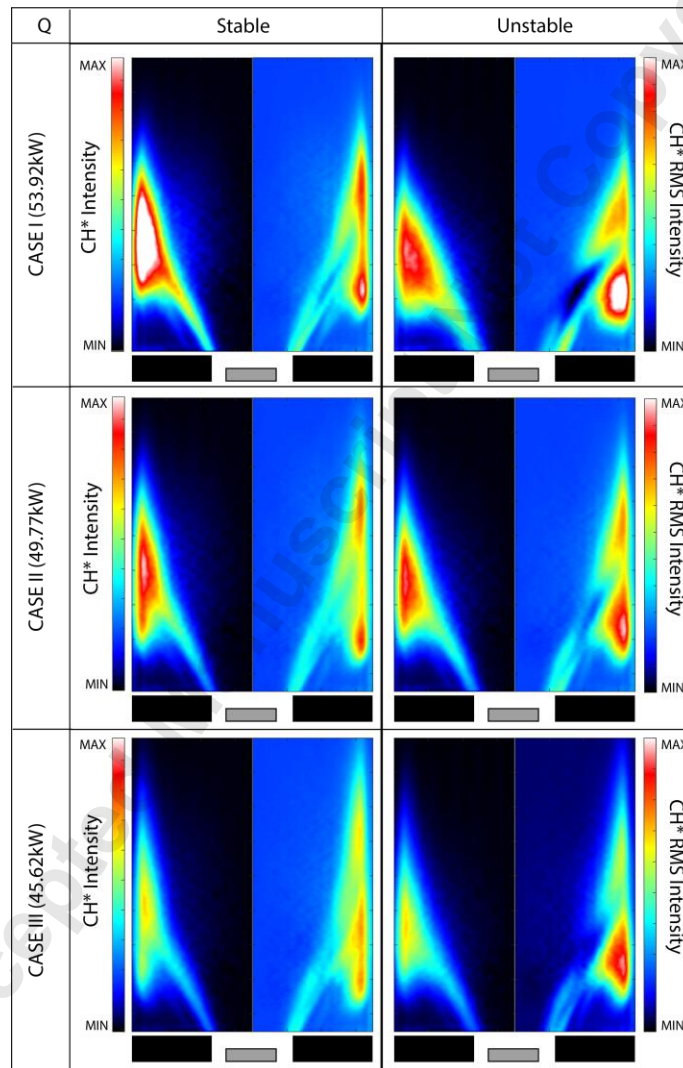


Figure 3. CH* images for Case I (top), Case II (middle), and Case III (bottom) showing the time-averaged, Abel-inverted flame structure (left) and RMS fluctuation level (right).

Flame center of heat release rate analysis for stable cases showed that each case has similar locations for centers of heat release rate despite having different heat rates and hydrogen percentages; tabulated center of heat release rate results can be seen in Table 3. Case I had the closest center of heat release rate to the nozzle, followed by Case II, then Case III. This order can be expected, since lower heat rate generally yields lower reactivity and flame speeds. This reduction in heat rate and reactivity causes flame length increases, which push the distribution of heat release further downstream. The difference in center of heat release between Case II and Case III is smaller than that of Case I and Case II. This is likely due to the balance between the lower heat rate and higher hydrogen content of Case III. All transitions resulted in shifts in center of heat release rate further upstream in the combustor. This could be both a result of increased fluctuation of flame location as well as increases in hydrogen elevating the consumption speed of the flame, allowing the flame to exist lower in the combustor.

Table 3. Flame center of heat release rate calculations from images in Figure 2. Percent changes are relative to the stable position. Locations are relative to the bottom of the image (axial) and the centerline of the image (radial).

1 pixel = 0.3302mm		Radial (Pixels)	Radial (mm)	% Change	Axial (Pixels)	Axial (mm)	% Change
Case I	Stable	156.0	51.6		164.6	54.4	
	Unstable	147.9	48.8	-5.2	134.7	44.5	-18.2
Case II	Stable	154.6	51.1		173.8	57.4	
	Unstable	155.5	51.3	0.6	157.9	52.1	-9.1
Case III	Stable	152.9	50.5		178.2	58.9	
	Unstable	154.9	51.1	1.3	149.4	49.3	-16.2

Transient results

Each heat rate, transient direction, and transient timescale was run between 16 and 22 times over six different test days. Sample onset and decay transients can be seen in Figure 4. This figure shows the pressure trace, pressure envelope, and regression fits. It also shows that the envelope and regression are properly being fitted to the pressure data.

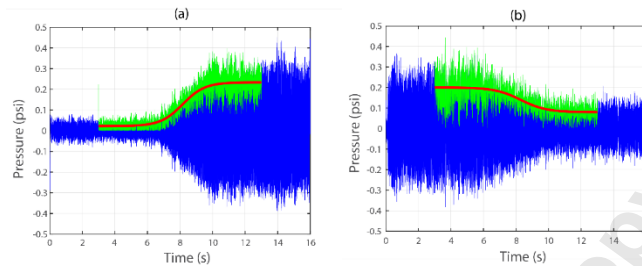


Figure 4. Sample pressure data for a 4 s onset (a) and decay (b) transient, showing pressure trace (blue), pressure envelope (green), and regression fit (red).

For each transient case, we initialize every test with a natural gas flame at the stable natural gas flow rate. After the natural gas flow was stabilized and a baseline centerbody temperature achieved, we actuated the solenoid valve to deliver the initial hydrogen flow to the experiment and then the controller varied this flow according to the prescribed transient schedule. The average uncertainty of the solenoid valve flow rates for these experiments was 2.677 SLPM hydrogen before the transient (equating to 14.83% of the nominal flow rate) and 3.661 SLPM hydrogen after the transient (equating to 24.18% of the nominal value). Since the natural gas flow is manually adjusted by a needle valve, the natural gas flow rate remained at the proper flow rate to match the stable combustor condition for every transient test. This was done to avoid manual adjustment of natural gas flow during a test and allowed us to quantify the effects of hydrogen fuel flow rate change. It also allowed us to automate fuel composition changes and capture hydrogen addition and subtraction effects. While these transient tests do not maintain constant heat rates as a result, we can effectively capture transitions to and from instability by matching the stable natural gas

flow rate and subsequently adding or subtracting hydrogen to achieve most closely the operating conditions measured from the stability map in Table 2.

Boxplots are used to quantify the combustor pressure fluctuations before and after the transient for all the tests. The red line indicates the median of the data, while the upper and lower bound of the box is the inner quartile range (IQR). The “whiskers” of each plot are shown as black lines and represent the maximum and minimum values of the data set. Values outside of a $1.5 \times \text{IQR}$ range are considered outliers and are plotted as red crosses. The notches on these plots represent the 95% confidence intervals on the median value [45]. Medians can be considered statistically significantly different at the 95% confidence interval if their notches do not overlap.

Case I: Flame Dynamics

Figure 5 shows the RMS combustor pressure fluctuations for the onset direction of Case I. For all RMS combustor pressure fluctuation boxplot figures, “I” represents the initial state and “F” represents the final state. Initial and final RMS values were calculated by taking the RMS of the first half and second half of the pressure envelope, respectively. Figure 5 indicates that the initial states for the 1 ms and 4 s transient cases are not statistically significantly different since their notches overlap. Conversely, the final states of the two different transient times are statistically significantly different; the 4 s transient times yield lower final state pressure fluctuation amplitudes for Case I.

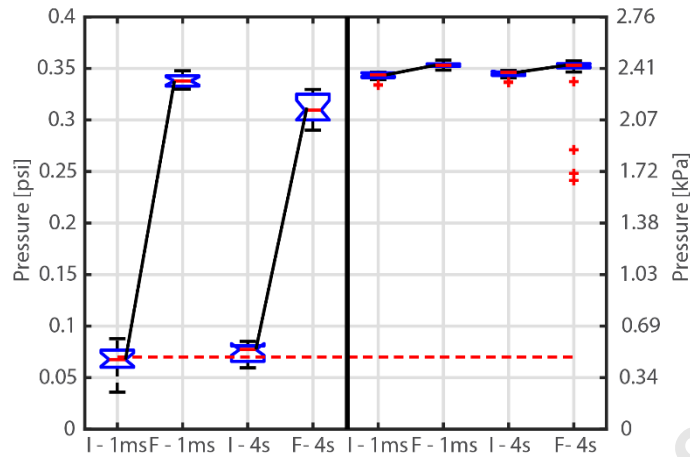


Figure 5. RMS combustor pressures before and after onset (left) and decay (right) transients for Case I.

Figure 5 also shows RMS combustor pressure fluctuations for the decay direction of Case I. Similar to the onset tests, the initial states of the two transient times are not statistically significantly different, but neither are the final states. Figure 5 also shows that despite a decrease in hydrogen flow over the duration of the transient, pressure oscillations appear to increase slightly, resulting in unexpected unstable operation. This amplitude increase is different than what was observed in the steady-state stability map. There are some outliers in the 4 s decay cases, however, that show a significant drop in the pressure amplitude after the transient.

Figure 6 shows example pressure time traces for Case I onset and decay transients. For the 1 ms onset cases, there is noticeable intermittency in pressure oscillation amplitude before the valve acts. When pressure oscillations are smaller, the flame is largely stationary, with minimal flame angle changes and variations in overall CH* emission. When larger pressure peaks occur during this intermittent time frame, flame angle changes increase in intensity as a result of vortices that propagate along the flame edge. The vortices eventually impinge on the combustor liner, resulting in larger emission of CH* in this area. During the intermittent time of the pressure trace, the flame

oscillates between these two states. Example film strips of these intermittent flame processes are shown in Figure 7(a), with red arrows highlighting key flame shape differences between the two cycles. Instantaneous images are used to show these flame processes as ensemble averaging is not possible in transient data.

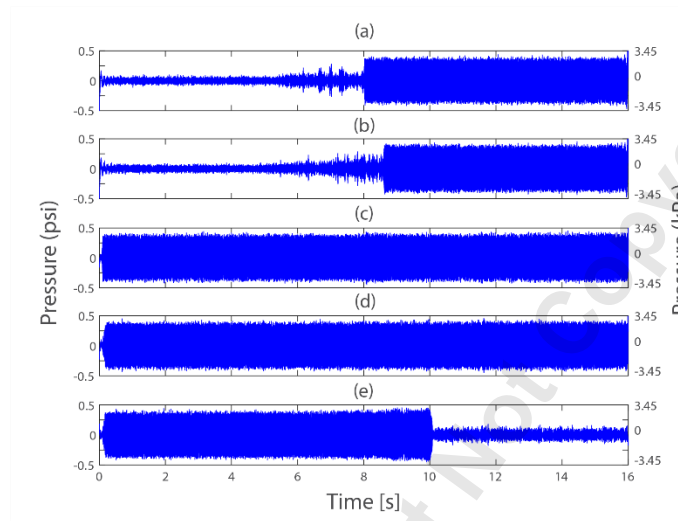


Figure 6. Combustor pressure for Case I onset (a-1 ms, b-4 s) and decay (c-1 ms, d-4 s, e-4 s forced).

When the combustor fully transitions to instability (after the valve acts at 8 s), larger scale flame angle changes occur, due to more intense vortex roll-up. As vortices strike the quartz combustor liner and roll into the recirculation zone, CH* intensity peaks in this area and combustion gases flow upstream into the recirculation zone. After the roll-up event, CH* intensity reduction occurs above this area, resembling a partial extinction event in the upper part of the flame. After the vortex impingement, the remaining gases propagate downstream, resulting in a flame length increase and further flame angle change originating from the nozzle exit.

For the 4 s onset case, similar intermittent behavior exists both before and as the valve acts. The mechanisms of the intermittent and unstable behavior are similar to that of the 1 ms onset case. However, one significant difference between the two transient times is that the 4 s transient

case appears to transition to instability over a longer timescale than the 1 ms case, which is expected given the actuation time of the valve. Similar instability onset through intermittency behavior was found by Nair et al. [46] in a backward-facing-step combustor. The work showed that intermittency events lasted longer as unstable operating conditions drew closer and that intermittency can be a precursor to combustion instability.

For the 1 ms decay cases, the instability mechanisms are similar to that of the onset cases in the form of vortex formation, large-scale flame angle changes, and CH* intensity reduction above the vortex impingement location. However, after the valve acts at 8 s, the instability mechanisms remain and the pressure oscillations appear to increase slightly. CH* intensity reduces slightly, likely due to the reduction of hydrogen flow. Similar behavior is observed for the 4 s decay transients.

To understand why the instability did not decay, we “forced” the system to undergo a transition by lowering the solenoid supply voltage of the final stage by 9.9%. This resembled roughly a 35% change in final stage hydrogen flow rate (which is greater than the uncertainty), as is seen in Figure 6(e). In this case, there is a noticeable increase in pressure oscillation amplitude over the duration of the transient, followed by significant reduction in pressure oscillation right as the solenoid valve finishes its adjustment to the new hydrogen flow rate. While the instability mechanisms were similar in the unstable portion of this case, they diminish after the transient reaches completion (after 10 s on the pressure trace). After the transient is complete, the flame appears stable.

One possible explanation for the lack of amplitude decay and transition to stability for Case I decay cases could be the increase in centerbody temperatures during the unstable portion of the test. Since the heat rate is the highest for this case, centerbody temperatures are considerably higher by the end of the instability period due to the high levels of oscillation and the proximity of the

flame center of heat release to the centerbody, as shown in Table 3. These elevated centerbody temperatures can be seen in Figure 8. The figure shows that the centerbody temperatures at the end of the transient test are considerably higher in the decay direction. Because of the elevated temperatures in the decay direction, the combustor may be more prone to instability, as demonstrated by Westfall et al. [47] in this same experiment and Hong et al. [48] in a backwards-facing step configuration. As a result, the combustor may require a more significant reduction in hydrogen flow to cause stable operation. This increased propensity to remain unstable would explain why the forced transient for Case I was more successful than the others, as it may have overcome the hysteretic behavior of the system that was caused by the thermal lag in the flame stabilization boundary condition.

Accepted Manuscript Not Copyable

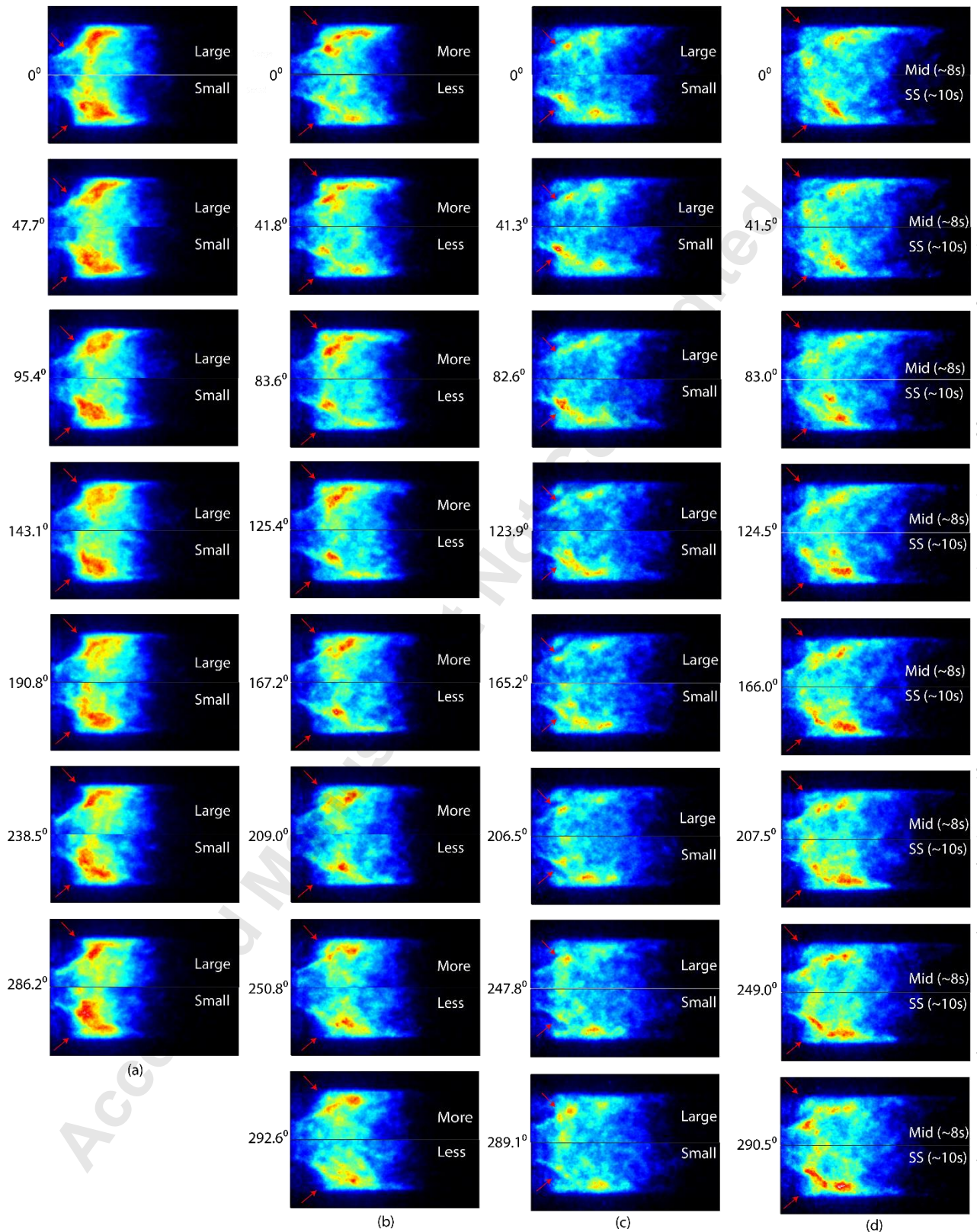


Figure 7. CH* images for Case I: intermittent behavior prior to 1 ms onset transient showing large and small flame shape changes (a), Case II: more and less variation in vortex intensity O' for 1 ms onset transient (b), Case III: large and small fluctuation seen during the ~0.2 s after the 1 ms onset transient (c), and Case III: mid-range oscillation cycle (~8 s) and steady-state

unstable state (~10 s) for the 4 s onset transient (d)

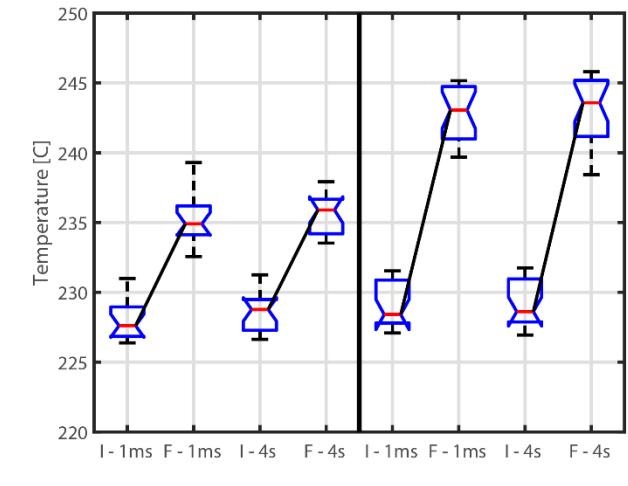


Figure 8: Centerbody temperatures at the beginning “I” and end “F” of each transient test for the onset (left) and decay (right) direction of Case I.

Case II: Flame Dynamics

Figure 9 shows RMS combustor pressure fluctuations for the onset direction of Case II. Neither the initial nor final states of the transient are statistically significantly different for the 1 ms and 4 s cases, indicating the insensitivity of this operating case to transient times. One difference between this case and Case I is the much wider distribution of final pressure oscillation amplitudes at both timescales.

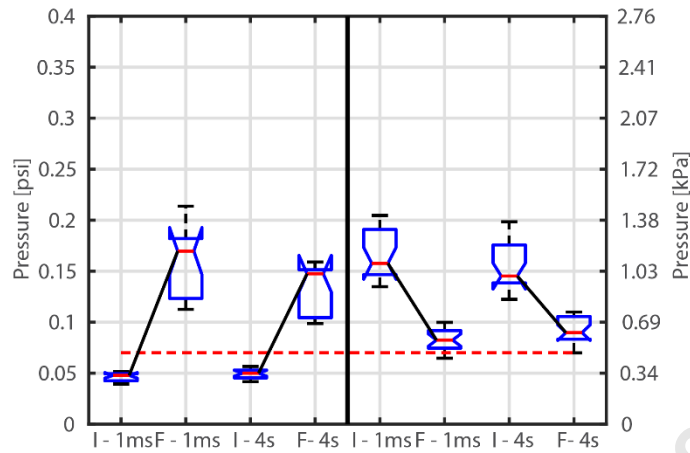


Figure 9. RMS combustor pressures before and after onset (left) and decay (right) transients for Case II.

Figure 9 also shows RMS combustor pressure fluctuations for the decay direction of Case II. Like the onset cases, the initial and final states of the transient are not statistically significantly different for the 1 ms and 4 s cases. The initial instability amplitudes in the decay cases have a similar spread to the final instability amplitudes in the onset cases, which indicates that the variation in the instability amplitude from test to test in the onset cases is not a result of the transient itself, but instead suggests that this operating condition is close to the stability bifurcation point. The variation in the instability amplitude between tests may be a result of heightened sensitivity of the instability to the bifurcation parameter, here the hydrogen mole fraction, as compared to the operating conditions in Case I.

Figure 10 shows example pressure time traces for Case II onset and decay transients. For the 1 ms onset cases, the pressure oscillations are fairly consistent in the stable state; there is noticeably less intermittency in the Case II stable state than in the Case I stable state. As the valve acts at 8 s, flame angle changes immediately grow more intense, as larger vortices form and propagate toward the outer recirculation zone. When the vortices reach the outer recirculation zone, they impinge on the liner farther downstream and do not propagate as far upstream after impingement as they do in

Case I. This can be expected due to the lower heat rate of Case II, resulting in a taller flame due to lower reactivity and flame speeds than Case I. After vortex impingement, there is a similar CH^* intensity reduction above the impingement location as seen in Case I, but the intensity reduction is less significant. Another significant difference in the Case II unstable state is that there is considerable variation in the vortex impingement location during a given pressure oscillation cycle. Vortices that propagate further into the recirculation zone after impingement generally have a higher CH^* fluctuation intensity due to the stronger recirculation of reactants into the corner recirculation zone. This variation in the impingement location is shown in the filmstrip in Figure 7(b), where the top images show a more intense case and the bottom images show a less intense case. Red arrows point to the impingement locations for each image set and highlight the differences in overall intensity in the impingement zone.

This variation in vortex impingement location and flame fluctuation intensity could be a result of vortex jitter [49] and can be seen in the form of varying pressure oscillation amplitude throughout the unstable portion of the pressure trace in Figure 10. During this time, there are periods when the flame appears almost stable due to the jitter of the flame. Because the pressure oscillation amplitudes are significantly lower in Case II than Case I, pressure disturbances are causing smaller velocity disturbances at the nozzle exit, which results in lower vortex strength, as was shown by Mathews et al. [50] in a swirling flow with similar swirl number.

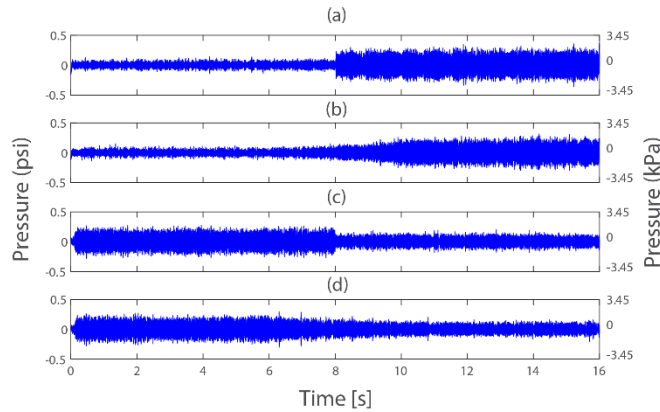


Figure 10. Combustor pressure for Case II onset (a-1 ms, b-4 s) and decay (c-1 ms, d-4 s).

The 4 s onset cases have similar unstable states as compared to the 1 ms onset cases. The main difference between the two flame behaviors can be seen in the pressure traces, where the 4 s transients result in more gradual pressure oscillation amplitude increases, as would be expected given the actuation time of the valve. The unstable state also has similar flame dynamics to the unstable state of the 1 ms transient.

For the 1 ms decay cases, the unstable state mechanisms are similar to that of the onset cases. After the solenoid valve acts at 8 s, there are noticeable overall reductions in pressure oscillation amplitude. This transition corresponds to less intense flame angle changes and vortex roll-up. In addition, vortex roll-up appears to happen less frequently and bulk flame CH^* intensity fluctuations across the entire flame appear to become more dominant than the periodic convective disturbances seen during instability. These bulk intensity fluctuations appear to originate from the nozzle exit, where there are periods of time that the nozzle exit significantly reduces in CH^* intensity. These high-intensity fluctuations likely cause more reactants to propagate toward the outer recirculation zone. When the reactants reach the outer recirculation zone, they ignite, causing the entire flame to appear more intense. Following this sudden increase in intensity, there is also a decrease in intensity directly afterward. The 4 s decay transients show similar initial and final state

behavior, with a more gradual decrease in pressure oscillation amplitude and occasional periods of more stable flame behavior.

Unlike the Case I decay cases, the Case II decay cases do result in a reduction in instability amplitude, though it does not decrease to the same level as the initial stable amplitude of the onset cases. This result indicates that the reduction in hydrogen does overcome the stability bifurcation, unlike in Case I, but that the temperature of the centerbody likely still plays a role as the amplitude of the stable section is relatively high. Centerbody temperatures for Case II can be seen in Figure 11. The figure clearly shows elevated temperatures in the decay direction, but not as significant a difference as seen in Case I.

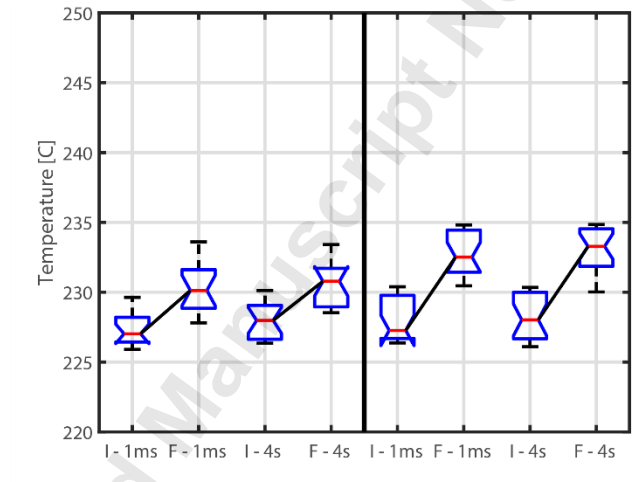


Figure 11: Centerbody temperatures at the beginning “I” and end “F” of each transient test for the onset (left) and decay (right) direction of Case II.

Case III: Flame Dynamics

Figure 12 shows RMS combustor pressure oscillations for Case III onset, where the final states are not statistically significantly different between the 1 ms and 4 s cases. These results also show consistent increases in pressure oscillation amplitude over the course of both onset transient

timescales. Figure 12 also shows RMS combustor pressure fluctuations for Case III decay cases, indicating that for both transient times, initial states are only slightly different from their respective final states. Case III decay was not successful in significantly reducing pressure oscillation amplitude or stabilizing the combustor. This is likely due to increased centerbody temperatures in the decay direction, as seen in Figure 13. The figure clearly shows elevated final temperatures in the decay direction. The figure also shows that differences in final centerbody temperatures for Case III are greater than that of Case II, but less than that of Case I.

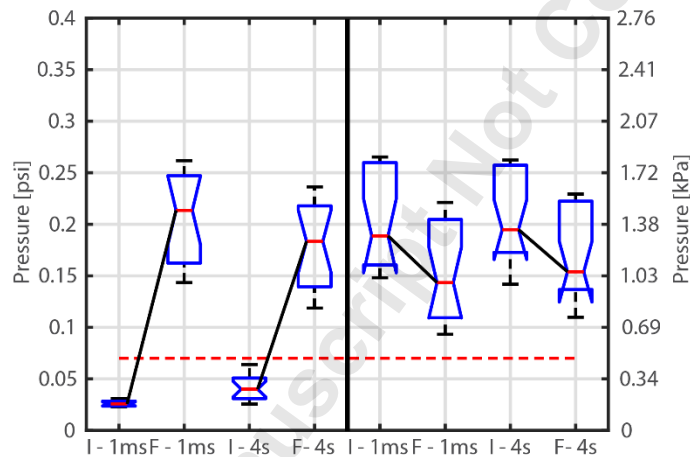


Figure 12. RMS combustor pressures before and after onset (left) and decay (right) transients for Case III.

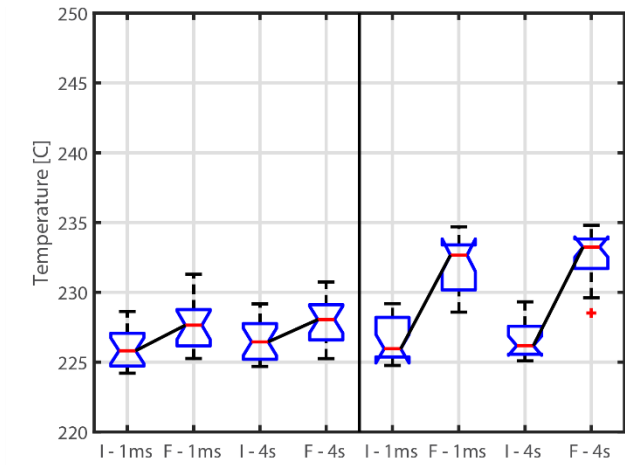


Figure 13: Centerbody temperatures at the beginning “I” and end “F” of each transient test for the onset (left) and decay (right) direction of Case III.

Figure 14 shows example pressure time traces for Case III onset and decay transients. For the 1 ms onset cases (Figure 14(a)), flame imaging during the stable state shows minimal flame angle changes and consistent recirculation zone location, which is reflected in the relatively low intermittency pressure signal before the transient. As the valve acts at 8 s, pressure oscillation amplitude immediately increases. This corresponds to dramatic flame length decrease as more hydrogen is added to the flame. As the flame transitions to unstable operation, considerable flame angle changes and vortex formation results. In this small transition region where the pressure oscillation amplitude appears considerably higher than the steady-state unstable amplitude, there are also noticeable transitions between large unstable flame oscillations and brief apparently stable states. These states are shown in the filmstrip in Figure 7(c), where the large oscillations are on the top of the figure, and the small oscillations are on the bottom of the figure. Red arrows highlight the differences in overall intensity fluctuation between these two states. The film strips show significant intensity increase in the highlighted region of the larger fluctuation state, and more constant intensity in this region for the smaller fluctuation state over the course of the cycle. While

the unstable states yield larger pressure oscillations, the brief stable states yield considerably low-pressure oscillations, smaller flame angle changes, and smaller vortex formations. This alternation between periods of large and small pressure amplitude oscillations continues for roughly 0.2 s.

After this point, the flame settles into a smaller amplitude pressure oscillation cycle. In the unstable state, vortices impinge on the liner farther upstream into the outer recirculation zone than in Case II, but not as far upstream as in Case I. In addition, vortices appear to curl more tightly into the recirculation zone than in Case II, but not as tightly as in Case I. After vortices impinge, CH* intensity increases in this area, followed by CH* intensity decreases above this area, likely due to flame extinction from the flame impingement on the wall. Variations in flame angle changes and vortex impingement location also occur, which likely correspond to less consistent pressure oscillation amplitudes in the unstable state.

The 4 s transient times yield similar stable flame behavior and pressure trace behavior. As the solenoid valve acts between 6 s and 10 s, the slower addition of hydrogen causes a slower increase in pressure oscillation amplitude. The final unstable state is similar to the 1 ms case. The 4 s transient times appear to lack the brief period of larger pressure oscillation, likely due to the more gradual change in hydrogen flow rate. Flame oscillation behavior during this slow transient is shown in Figure 7(d) during two portions of the transient. Red arrows highlight zones of intensity differences, likely resulting in differences in overall pressure fluctuation amplitude. The flame for the mid-range cycle also appears longer, likely due to this cycle's smaller hydrogen flow rate. By the time the steady-state instability is reached, more hydrogen is flowing, causing the flame to shorten.

For 1 ms decay cases, unstable state flame behaviors are similar to that of the onset cases. When the valve acts at 8 s, there is a significant reduction in pressure oscillation amplitude,

followed by an increase in pressure amplitude, resulting in a final state that has only a slightly lower pressure oscillation than the initial state. Immediately after the valve acts, the significant reduction in pressure amplitude corresponds to a much more stable flame. After this short time, vortex formation and impingement intensity increase. Flame fluctuations appear less intense than the initial states. The final state also shows more prominent bulk CH^* fluctuation, particularly near the flame attachment point at the nozzle. The 4 s transient decay initial and final states are similar, but the transitions are different. 4 s transient cases show more gradual reduction in pressure oscillation amplitude and there is no “dip” in pressure oscillation amplitude before the final state is reached.

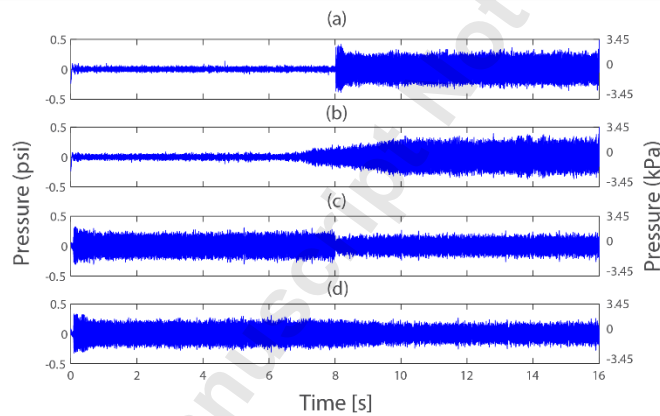


Figure 14. Combustor pressure for Case III onset (a-1 ms, b-4 s) and decay (c-1 ms, d-4 s).

CONCLUSIONS

This paper describes the effects of steady-state and transient hydrogen-enrichment on thermoacoustic instability in a model gas turbine combustor. A steady-state stability map was used to quantify combustor operating states over a range of hydrogen-natural gas fuel blends and a range of heat rates. Steady-state tests show that both heat rate and hydrogen content affect system stability. At a given heat rate, increasing levels of hydrogen result in unstable combustion. As heat rate increases, instability occurs at lower concentrations of hydrogen in the fuel. Analysis of time-

averaged and RMS CH* images revealed that adding hydrogen causes flame length to reduce and flame shape to change, which then corresponds to changes in flame stability. Case I showed the most dramatic shift in center of heat release rate location, followed by Case III, and then Case II.

Transient operation was tested in the onset and decay directions, with two hydrogen transient times – a short time of 1 millisecond and a long time of 4 seconds. Results show that instability onset processes were more repeatable (regardless of timescale). However, certain instability decay processes are less repeatable, resulting in cases that do not fully transition from unstable to stable combustion despite similar changes in hydrogen flow rate. This lack of transition is likely the result of hysteresis driven by the thermal boundary condition at the flame attachment point on the centerbody. After the instability, the centerbody is much hotter, which tends to encourage instability. In the onset cases, the flame centerbody temperature does not increase so dramatically before the transient operation and so the final instability state of the flame is not as affected.

For Case I onset, initial states were not statistically significantly different for 1 ms and 4 s, but final states were. The 4 s transient times yielded consistently lower unstable amplitudes. For Case I decay, initial states were not statistically significantly different, and neither were the final states. Case I decay also showed slight increases in oscillation amplitude over the course of the transient. Investigation of a “forced” decay for Case I showed that slight increases in amplitude could be a precursor to a sharp decay upon further hydrogen reduction. Case II did not show significant hysteretic behavior or dependency on transient timescale.

For Case III onset, 4 s transients yielded consistently larger initial amplitudes. The 4 s transients also seemed to yield slightly lower final amplitudes, but the results did not yield statistical significance. For Case III decay, neither the initial states nor the final states were statistically significantly different between 1 ms and 4 s. In addition, results showed that Case III decay was

unsuccessful in oscillation amplitude reduction over the course of the transient, indicating potential hysteretic combustor behavior. Overall, the comparison of transient times between initial and final combustor states shows that when initial and final states are significantly different, 4 s transients yield smaller differences in pressure amplitudes, while 1 ms transients yield larger overall differences in pressure amplitude oscillation.

Investigation of high-speed CH* images for each case showed that the dominant instability mechanisms were flame angle changes, vortex impingement location changes, vortex intensity, periodic flame length changes due to extinction events above the vortex impingement location, and bulk flame CH* fluctuations. All of these mechanisms varied in intensity and prevalence depending on each case and each case's direction. These variations play a significant role in pressure oscillation amplitude and transition mechanisms across decay and onset transients. These variations are likely caused by the higher overall centerbody temperatures in the decay direction and lower overall centerbody temperatures in the onset direction. Similarly, flame dynamics differences between cases could be a result of heat rate differences having varying effects on centerbody temperature.

The implications of this work indicate that conjugate heat transfer predictions may be needed to correctly capture combustion instability, particularly in the case of transient operation. The importance of wall temperature boundary conditions on flame static and dynamic stability has been recognized in the literature [51–54], but mostly for steady-state operation. Recent work showing that heat transfer between the flame and the wall is important in transient operation [26,28], now shown with variation in fuel composition, confirms the importance of these multi-physics considerations in understanding thermoacoustic instability.

ACKNOWLEDGMENTS

This work was funded by the US Department of Energy University Turbine Systems Research Program under grant DE-FE0025495 with program monitor Mark Freeman.

REFERENCES

- [1] M. Moliere, “Benefiting from the Wide Fuel Capability of Gas Turbines: A Review of Application Opportunities,” in *ASME Turbo Expo 2002*.
- [2] T. Boushaki, Y. Dhué, L. Selle, B. Ferret, and T. Poinsot, “Effects of hydrogen and steam addition on laminar burning velocity of methane-air premixed flame: Experimental and numerical analysis,” *Int. J. Hydrogen Energy*, vol. 37, no. 11, pp. 9412–9422, 2012.
- [3] R. W. Schefer, “Hydrogen enrichment for improved lean flame stability,” *Int. J. Hydrogen Energy*, vol. 28, no. 10, pp. 1131–1141, 2003.
- [4] R. W. Schefer, D. M. Wicksall, and A. K. Agrawal, “Combustion of hydrogen-enriched methane in a lean premixed swirl-stabilized burner,” *Proc. Combust. Inst.*, vol. 29, no. 1, pp. 843–851, 2002.
- [5] H. M. Altay, R. L. Speth, D. E. Hudgins, and A. F. Ghoniem, “Flame – vortex interaction driven combustion dynamics in a backward-facing step combustor,” *Combust. Flame*, vol. 156, no. 5, pp. 1111–1125, 2009.
- [6] S. Ducruix, T. Schuller, D. Durox, and S. Candel, “Combustion Dynamics and Instabilities : Elementary Coupling and Driving Mechanisms,” *J. Propuls. Power*, vol. 19, no. 5, pp. 722–734, 2003.
- [7] P. Palies, D. Durox, T. Schuller, and S. Candel, “The combined dynamics of swirler and turbulent premixed swirling flames,” *Combust. Flame*, vol. 157, no. 9, pp. 1698–1717,

- 2010.
- [8] T. Sattelmayer, “Influence of the Combustor Aerodynamics on Combustion Instabilities From Equivalence Ratio Fluctuations,” *J. Eng. Gas Turbines Power*, vol. 125, pp. 11–19, 2003.
- [9] S. Hong, S. J. Shanbhogue, R. L. Speth, and A. F. Ghoniem, “On the Phase between Pressure and Heat Release Fluctuations for Propane / hydrogen Flames and Its Role in Mode Transitions,” *Combust. Flame*, vol. 160, no. 12, pp. 2827–2842, 2013.
- [10] M. C. Lee, J. Yoon, S. Joo, J. Kim, J. Hwang, and Y. Yoon, “Investigation into the cause of high multi-mode combustion instability of H₂/CO/CH₄ syngas in a partially premixed gas turbine model combustor,” *Proc. Combust. Inst.*, vol. 35, no. 3, pp. 3263–3271, 2015.
- [11] N. A. Baraiya and S. R. Chakravarthy, “Effect of syngas composition on high frequency combustion instability in a non-premixed turbulent combustor,” *Int. J. Hydrogen Energy*, vol. 44, no. 12, pp. 6299–6312, 2019.
- [12] D. W. Davis, P. L. Therkelsen, D. Littlejohn, and R. K. Cheng, “Effects of hydrogen on the thermo-acoustics coupling mechanisms of low-swirl injector flames in a model gas turbine combustor,” *Proc. Combust. Inst.*, vol. 34, no. 2, pp. 3135–3143, 2013.
- [13] J. Zhang and A. Ratner, “Experimental study on the excitation of thermoacoustic instability of hydrogen-methane/air premixed flames under atmospheric and elevated pressure conditions,” *Int. J. Hydrogen Energy*, vol. 44, no. 39, pp. 21324–21335, 2019.
- [14] T. García-Armingol, Á. Sobrino, E. Luciano, and J. Ballester, “Impact of fuel staging on stability and pollutant emissions of premixed syngas flames,” *Fuel*, vol. 185, pp. 122–132, 2016.
- [15] G. S. Jackson, R. Sai, J. M. Plaia, C. M. Boggs, and K. T. Kiger, “Influence of H₂ on the

- response of lean premixed CH₄ flames to high strained flows,” *Combust. Flame*, vol. 132, no. 3, pp. 503–511, 2003.
- [16] R. L. Speth and A. F. Ghoniem, “Impact of Hydrogen Addition on Flame Response to Stretch and Curvature,” in *43rd AIAA Aerospace Sciences Meeting and Exhibit*, 2005.
- [17] D. Michaels, S. J. Shanbhogue, and A. F. Ghoniem, “The impact of reactants composition and temperature on the flow structure in a wake stabilized laminar lean premixed CH₄/H₂/air flames; mechanism and scaling,” *Combust. Flame*, vol. 176, pp. 151–161, 2017.
- [18] F. Halter, C. Chauveau, and I. Gökalp, “Characterization of the effects of hydrogen addition in premixed methane/air flames,” *Int. J. Hydrogen Energy*, vol. 32, no. 13, pp. 2585–2592, 2007.
- [19] D. M. Wicksall, A. K. Agrawal, R. W. Schefer, and J. O. Keller, “The interaction of flame and flow field in a lean premixed swirl-stabilized combustor operated on H₂/CH₄/air,” *Proc. Combust. Inst.*, vol. 30, no. 2, pp. 2875–2883, 2005.
- [20] S. Hong, S. J. Shanbhogue, and A. F. Ghoniem, “Impact of fuel composition on the recirculation zone structure and its role in lean premixed flame anchoring,” *Proc. Combust. Inst.*, vol. 35, no. 2, pp. 1493–1500, 2015.
- [21] D. M. Wicksall and A. K. Agrawal, “Influence of Hydrogen Addition on Flow Structure in Confined Swirling Methane Flame,” *J. Propuls. Power*, vol. 21, no. 1, pp. 16–24, 2005.
- [22] L. Figura, J. G. Lee, B. D. Quay, and D. A. Santavicca, “The Effects of Fuel Composition on Flame Structure and Combustion Dynamics in a Lean Premixed Combustor,” in *ASME Turbo Expo 2007*.
- [23] O. Tuncer, S. Acharya, and J. H. Uhm, “Dynamics, NO_x and flashback characteristics of

- confined premixed hydrogen-enriched methane flames,” *Int. J. Hydrogen Energy*, vol. 34, no. 1, pp. 496–506, 2009.
- [24] T. Lieuwen, V. McDonell, E. Petersen, and D. Santavicca, “Fuel Flexibility Influences on Premixed Combustor Blowout, Flashback, Autoignition, and Stability,” *J. Eng. Gas Turbines Power*, vol. 130, no. 1, p. 011506, 2008.
- [25] M. W. Melaina, O. Antonia, and M. Penev, “Blending Hydrogen into Natural Gas Pipeline Networks: A Review of Key Issues,” *NREL Technical Report*, vol. NREL/TP-56. 2013.
- [26] G. Bonciolini, D. Ebi, U. Doll, M. Weilenmann, and N. Noiray, “Effect of wall thermal inertia upon transient thermoacoustic dynamics of a swirl-stabilized flame,” *Proc. Combust. Inst.*, vol. 37, no. 4, pp. 5351–5358, 2019.
- [27] G. Bonciolini and N. Noiray, “Bifurcation dodge: avoidance of a thermoacoustic instability under transient operation,” *Nonlinear Dyn.*, vol. 96, no. 1, pp. 703–716, 2019.
- [28] W. Culler, X. Chen, J. Samarasinghe, S. Peluso, D. Santavicca, and J. O’Connor, “The effect of variable fuel staging transients on self-excited instabilities in a multiple-nozzle combustor,” *Combust. Flame*, vol. 194, pp. 472–484, 2018.
- [29] X. Chen, W. Culler, S. Peluso, D. Santavicca, and J. O’Connor, “Comparison of Equivalence Ratio Transients on Combustion Instability in Single-Nozzle and Multi-Nozzle Combustors,” in *ASME Turbo Expo 2018*.
- [30] I. Boxx, C. D. Carter, K. P. Geigle, W. Meier, B. Akih-Kumgeh, and J. Lewalle, “A Study of Spontaneous Transition in Swirl-Stabilized Flames,” in *ASME Turbo Expo 2017*.
- [31] T. M. Wabel, M. Passarelli, J. D. Maxim Cirtwill, P. Saini, A. M. Steinberg, and K. Venkatesan, “Measurements of the initial growth of thermoacoustic oscillations from noise in a model aeronautical combustor,” in *AIAA SciTech Forum*, 2018, pp. 1–12.

- [32] X. Chen, W. Culler, S. Peluso, D. Santavicca, and J. O'Connor, "Effects of the equivalence ratio transient durations on self-excited combustion instability time scales in a single nozzle combustor," in *Spring Technical Meeting Eastern States Section of the Combustion Institute*, 2018, pp. 1–8.
- [33] W. Culler, J. Samarasinghe, B. D. Quay, D. A. Santavicca, and J. O'Connor, "The Effect of Transient Fuel Staging on Self-Excited Instabilities in a Multi-Nozzle Model Gas Turbine Combustor," in *ASME Turbo Expo 2017*.
- [34] J. Samarasinghe, W. Culler, B. D. Quay, D. A. Santavicca, and J. O'Connor, "The Effect of Fuel Staging on the Structure and Instability Characteristics of Swirl-Stabilized Flames in a Lean Premixed Multinozzle Can Combustor," *J. Eng. Gas Turbines Power*, vol. 139, no. 12, p. 12154, 2017.
- [35] S. Barbosa, M. de La Cruz Garcia, S. Ducruix, B. Labegorre, and F. Lacas, "Control of combustion instabilities by local injection of hydrogen," *Proc. Combust. Inst.*, vol. 31, no. 2, pp. 3207–3214, 2007.
- [36] J. Samarasinghe, S. J. Peluso, B. D. Quay, and D. A. Santavicca, "The Three-Dimensional Structure of Swirl-Stabilized Flames in a Lean Premixed Multinozzle Can Combustor," *J. Eng. Gas Turbines Power*, vol. 138, no. 3, 2016.
- [37] A. J. De Rosa, S. J. Peluso, B. D. Quay, and D. A. Santavicca, "The Effect of Confinement on the Structure and Dynamic Response of Lean-Premixed, Swirl-Stabilized Flames," *J. Eng. Gas Turbines Power*, vol. 138, no. 6, pp. 1–10, 2016.
- [38] D. Fanaca, P. R. Alemela, C. Hirsch, and T. Sattelmayer, "Comparison of the flow field of a swirl stabilized premixed burner in an annular and a single burner combustion chamber," *J. Eng. Gas Turbines Power*, vol. 132, no. 7, pp. 1–7, 2010.

- [39] P. Orawannukul, “An experimental study of forced flame response in technically premixed flames in a lean premixed gas turbine combustor.” PhD Thesis: The Pennsylvania State University, 2014.
- [40] A. D. Pierce and R. T. Beyer, *Acoustics: An Introduction to Its Physical Principles and Applications*. Acoustical Society of America, 1981.
- [41] J. G. Lee and D. A. Santavicca, “Experimental Diagnostics of Combustion Instabilities,” in *Combustion Instabilities in Gas Turbine Engines: Operational Experience, Fundamental Mechanisms, and Modeling*, vol. 210, T. C. Lieuwen and V. Yang, Eds. 2005, pp. 481–529.
- [42] N. A. Bunce, “Flame Transfer Function Measurements and Mechanisms in a Single-Nozzle Combustor.” PhD Thesis: The Pennsylvania State University, 2013.
- [43] R. J. Kee, F. M. Rupley, E. Meeks, and J. A. Miller, *CHEMKIN-III: A Fortran Chemical Kinetics Package for the Analysis of Gas-Phase Chemical and Plasma Kinetics*, no. May. 1996.
- [44] G. P. Smith *et al.*, “GRI-Mech 3.0.” [Online]. Available: http://www.me.berkeley.edu/gri_mech/.
- [45] R. McGill, J. W. Tukey, and W. A. Larsen, *Variations of Box Plots*, vol. 32, no. 1. 1978.
- [46] V. Nair, G. Thampi, and R. I. Sujith, “Intermittency route to thermoacoustic instability in turbulent combustors,” *J. Fluid Mech.*, vol. 756, pp. 470–487, 2014.
- [47] S. Westfall, O. Sekulich, W. Culler, S. Peluso, and J. O’Connor, “Quantification of Intermittency in Combustion Instability Amplitude in a Multi-Nozzle Can Combustor,” in *ASME Turbo Expo*, 2020.
- [48] S. Hong, S. J. Shanbhogue, K. S. Kedia, and A. F. Ghoniem, “Impact of the Flame-Holder Heat-Transfer Characteristics on the Onset of Combustion Instability,” *Combust. Sci.*

- Technol.*, vol. 185, no. 10, pp. 1541–1567, 2013.
- [49] S. J. Shanbhogue, M. Seelhorst, and T. Lieuwen, “Vortex Phase-Jitter in Acoustically Excited Bluff Body Flames,” *Int. J. Spray Combust. Dyn.*, vol. 1, no. 3, pp. 365–387, 2009.
- [50] B. Mathews, S. Hansford, and J. O’Connor, “Impact of Swirling Flow Structure on Shear Layer Vorticity Fluctuation Mechanisms,” in *ASME Turbo Expo*, 2016.
- [51] P. Schmitt, T. Poinso, B. Schuermans, and K. P. Geigle, “Large-eddy simulation and experimental study of heat transfer, nitric oxide emissions and combustion instability in a swirled turbulent high-pressure burner,” *J. Fluid Mech.*, vol. 570, pp. 17–46, 2007.
- [52] D. Mejia, L. Selle, R. Bazile, and T. Poinso, “Wall-temperature effects on flame response to acoustic oscillations,” *Proc. Combust. Inst.*, vol. 35, no. 3, pp. 3201–3208, 2015.
- [53] S. J. Shanbhogue, Y. S. Sanusi, S. Taamallah, M. A. Habib, E. M. A. Mokheimer, and A. F. Ghoniem, “Flame macrostructures, combustion instability and extinction strain scaling in swirl-stabilized premixed CH₄ / H₂ combustion,” *Combust. Flame*, vol. 163, pp. 494–507, 2016.
- [54] P. D. Ronney, “Analysis of non-adiabatic heat-recirculating combustors,” *Combust. Flame*, vol. 135, no. 4, pp. 421–439, 2003.